Striking a Balance: Exploring Optimal Functionalities and Composition of Highly Adhesive and Dispersing Binders for High-Nickel Cathodes in Lithium-Ion Batteries

Daun Jeong, Da-Sol Kwon, Hee Joong Kim, and Jimin Shim**

Nickel-rich layered oxide, $LiNi_xCo_yMn_zO_2$ (NCM, $x > 0.8$), has emerged as a promising cathode material for lithium-ion batteries due to its high specific capacity and energy density. However, there remains a challenge regarding NCM degradation during cycling, associated with interfacial side reactions and microcrack formation. Herein, a functional poly(norbornene-*co*-norbornene dicarboxylic acid-*co*-heptafluorobutyl norbornene imide) (PNCI)-based binder system is introduced, with controlled functionalities and monomer compositions, to preserve the structural integrity of NCM. The PNCI binder system incorporates three different norbornene-derived monomers with distinct functionalities, allowing for multifunctionality, including electro-chemo-mechanical stability, strong adhesion, and dispersibility. By systematically adjusting the molar composition of the PNCI binders, the overall binder characteristics are fine-tuned, optimizing the adhesion and dispersion of electrode components. The optimized PNCI binder, with desired adhesion strength, surface energy, and polarity, plays a crucial role in facilitating the formation of a uniform electrode structure with a high areal mass loading of NCM, ensuring long-term cycling stability. This study highlights the significance of striking a balance between functionalities and composition in binder systems to achieve high-performance NCM cathodes.

1. Introduction

The ever-increasing demand for high-energy-density and long-lasting rechargeable lithium -ion batteries in the era of electric vehicles has spurred extensive research on high-energy-density cathode materials.[1–5] One material that has gained significant attention is the nickel-rich layered oxide, $LiNi_xCo_yMn_zO_2$ (NCM), due to its high energy density and specific capacity (> 200 mAh g^{-1}).[6,7] The high specific capacity is attributed to the presence of a $Ni^{3+/4+}$ e_g band positioned above the $2p$ band of O^{2-}, allowing for effective Li-ion storage utilizing $Ni^{3+/4+}$ species.[8,9] However, the elevated Ni content adversely affects the cycling stability of NCM, primarily due to the high reactivity of $Ni^{3+/4+}$ ionic species, which lead to the decomposition of carbonate-based electrolytes.[10,11] Additionally, the reduction of $Ni^{3+/4+}$ to Ni^{2+} triggers the migration of Ni^{2+} ions from their designated transition metal (TM) layer to the Li^+ layer within the crystal lattice. This migration, driven by the proximity of the ionic radii of Li^+ (0.76 Å) and Ni^{2+} (0.69 Å), results in cation mixing and the irreversible formation of a resistive NiO-type rock-salt phase.[12,13] The cation mixing induces internal strains and anisotropic volume changes, leading to the formation of intergranular cracks in the NCM particles. Consequently, the parasitic cycling accelerates the electrolyte decomposition and further pulverization of the NCM, which in turn leading to significant capacity fading upon cycling.[14,15]

To address the degradation issues of NCM, extensive researches have focused on modifying both the bulk and surface chemistry of NCM particles, aiming to preserve the layered lattice structure of NCM, thereby improving cycling stability. These efforts encompass various strategies such as introducing a

---

D. Jeong, D.-S. Kwon, J. Shim
Energy Storage Research Center
Korea Institute of Science and Technology (KIST)
14 Gil 5 Hwarang-ro, Seongbuk-gu, Seoul 02792, Republic of Korea
E-mail: jiminshim@snu.ac.kr

D.-S. Kwon
Department of Chemical and Biological Engineering
Korea University
145 Anam-ro, Seongbuk-gu, Seoul 02841, Republic of Korea

H. J. Kim
Department of Polymer Science and Engineering & Program in Environmental and Polymer Engineering
Inha University
100 Inha-ro, Michuhol-gu, Incheon 22212, Republic of Korea
E-mail: heejoong@inha.ac.kr

J. Shim
Department of Chemistry Education
Seoul National University
1 Gwanak-ro, Gwanak-gu, Seoul 08826, Republic of Korea

The ORCID identification number(s) for the author(s) of this article can be found under https://doi.org/10.1002/aenm.202302845

DOI: 10.1002/aenm.202302845

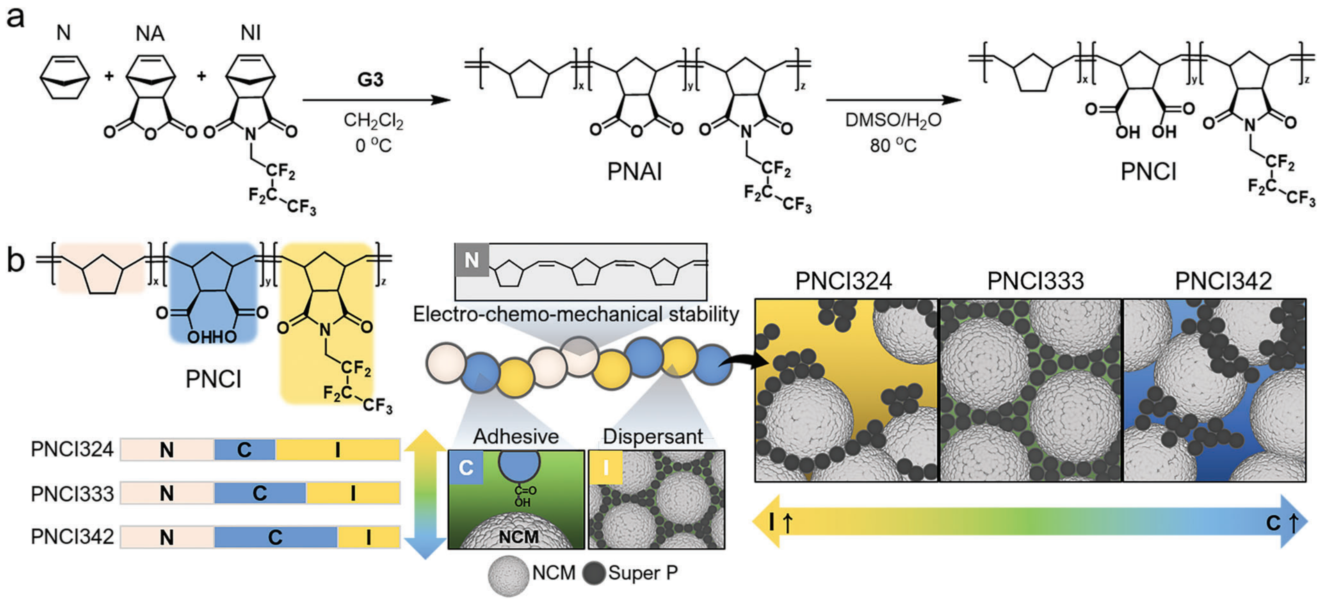

Figure 1. a) Synthesis of PNCI terpolymers and b) schematics highlighting the functional contributions of individual moieties in the PNCI# binder system.

concentration gradient of Ni,[16,17] doping with foreign atoms,[18,19] and applying surface coatings with inorganic materials.[20,21] In addition to NCM engineering approaches, judicious selection of highly adhesive binder materials holds great significance to retain the structural integrity of NCM because the binder plays an indispensable role in protecting NCM particles against the detrimental electrolyte decomposition, microcrack formation, and TM migration.[10,12,21] Conventional fluorinated binders including polyvinylidene fluoride (PVDF) lack polar moieties that can enhance adhesion strength and stabilize TM ions in NCM. Accordingly, previous research efforts on developing binder materials for NCM cathodes have primarily dedicated to the adoption of polymers incorporating polar moieties such as hydroxyl,[22] carboxylic acid,[23,24] urethane,[25] and nitrile groups.[26] These polar functional groups enhance the adhesion of the binder to NCM and the Al current collector through hydrogen bonding, while also stabilizing the surface TM ions of NCM through chelation, effectively mitigating the aforementioned degradation issues of NCM.[22,23,26,27]

Achieving uniform dispersion of the active materials, conductive carbon, and binder is another essential requirement for facilitating efficient ion and electron transport within the electrode, leading to superior cycling performance.[28,29] It is important to recognize that binders with excellent adhesion to the NCM active material, often characterized by high polarity, may experience reduced adhesion to low-polarity conductive carbon, resulting in a decrease in overall dispersibility of the electrode components. Since the various binder characteristics, including adhesion strength, dispersibility, and surface energy, collectively influence the interactions between the binder and the electrode components, balancing and optimizing the binder properties are important to obtain highly adhesive and dispersive NCM cathodes.[30] While individual aspects such as adhesion strength or dispersibility have been considered, the current state of binder research lacks sufficient emphasis on optimizing the overall binder properties to achieve the desired balance.[22,31–34]

Herein, we have developed a series of polynorbornene-based binders through ring-opening metathesis polymerization (ROMP), offering high molecular weight polymers with precise control over both molecular weights and monomer compositions. By incorporating three distinct norbornene-derived monomers with different functionalities, we have achieved multifunctionality, including electro-chemo-mechanical robustness, strong adhesion, and dispersibility, thus accessing desirable binder properties for NCM cathodes. Furthermore, the systematic variation in the molar composition of these monomers allows for delicate tuning of the binder properties including adhesion, surface energy, and polarity, enabling the optimization of binder characteristics to obtain highly adhesive and uniformly dispersed NCM cathodes. As a result, the well-balanced functional polynorbornene binder facilitates the formation of a highly uniform and integrated electrode structure, leading to high-performance NCM cathodes with high areal mass loading of active materials.

2. Results and Discussion

2.1. Design and Synthesis of PNCI# Binder System

A series of norbornene-based terpolymers, poly(norbornene-*co*-norbornene dicarboxylic acid-*co*-heptafluorobutyl norbornene imide) (PNCI#), was synthesized via straightforward ring-opening metathesis polymerization (ROMP) using multiple norbornene-derived monomers (**Figure 1**a). The number, #, indicates the feed molar ratio of norbornene (N), NA, and NI for the corresponding terpolymer. For example, PNCI324 represents the terpolymer synthesized with a feed molar ratio of N: NA: NI = 3:2:4. To obtain the PNCI terpolymers, a series of PNAI was synthesized by ROMP and subsequently hydrolyzed to convert the anhydride groups to dicarboxylic acid since direct polymerization of norbornene carboxylic acid is inhibited.[35,36] The molecular characteristics of the synthesized monomers and polymers were confirmed by ^{1}H and ^{13}C NMR spectroscopies and size exclusion chromatography (SEC) (Figures S1–S6 and Table S1, Supporting Information). Note that the molar masses of the PNCI#s were controlled within a narrow range of 448–461 kg mol^{-1} to ensure a fair comparison with the PVDF binder.[37] We intentionally targeted the high molecular weights within the controllable range to maximize cycling performance by achieving robust mechanical strength and strong adhesion properties.[37,38] As revealed by DSC, the T_g values of the PNCI#s were in the range of 39–48 °C, which ensures mechanical robustness at room temperatures (Figure S7, Supporting Information). Furthermore, the PNCI333 exhibited the highest toughness among the PNCI#s, primarily due to the balanced molar composition (Figure S8, Supporting Information). To understand the sequential distribution of monomeric units in a terpolymer, two sets of binary copolymerizations were performed, and the reactivity ratio values were determined using the Fineman-Ross method (Figure S9, Supporting Information).[39] The reactivity ratio values were found to be ≈1.0 for all monomers, indicating that the reactivity of each monomer is similar, yielding a statistical copolymer without any specific sequence or arrangement. Any slight differences are possibly attributed to the steric effect.[40] This result is consistent with the appearance of broad multiplet peaks in the ^{1}H NMR spectrum, derived from the methine protons (assigned as *a* in Figures S2–S4, Supporting Information).[41,42]

A series of PNCI#s with varying molar compositions of N, NA, and NI (N: NA: NI = 3:2:4, 3:3:3, and 3:4:2) was prepared to explore their suitability as binder materials for $LiNi_{0.8}Co_{0.1}Mn_{0.1}O_2$ (NCM811) cathodes (Figure 1b). Each monomeric unit was judiciously selected to introduce multiple functionalities that are advantageous for binder characteristics. The incorporation of a polynorbornene backbone in PNCI# imparts mechanical stability, primarily attributed to the cyclic structure. Additionally, the hydrocarbon-based backbone offers excellent electrochemical stability, particularly under high-voltage conditions.[43] The molar content of the norbornene (N) unit was carefully chosen as one-third of the total repeating units to ensure the solubility of PNCI#s in *N*-methyl-2-pyrrolidone (NMP) during the preparation of the cathode slurry. The nonpolar N unit enhances compatibility with the conductive carbon and prevents excessive swelling by liquid electrolytes, thereby promoting strong adhesion.[23] The presence of the carboxylic acid (C) unit enhances the adhesion to NCM and the Al current collector through hydrogen bonding, effectively protecting the NCM surface against interfacial side reactions and preventing detachment of the electrode composite layer from the Al current collector.[44] Furthermore, the C unit stabilizes the TM ions on the surface of NCM through chelation, suppressing TM migration and cracking of NCM.[23] The incorporation of the heptafluorobutyl imide (I) unit leads to a reduction in surface energy of PNCI#s primarily attributed to the inherently low surface energy of the perfluoroalkyl moiety.[45,46] This enables the I units to act as dispersants, effectively preventing the aggregation of NCM and conductive carbon particles, thereby achieving a highly dispersed electrode.[47] Another benefit of the perfluoroalkyl moieties is the promotion of Li-ion diffusion, potentially enhancing the ion-conduction through binders.[48] Note that imide linkage was employed to connect the norbornene backbone and perfluoroalkyl moiety due to its excellent electro-chemo-mechanical stability.[49–51] In addition to providing multiple functionalities to the PNCI system through the combination of three monomeric units, the systematic variation in the monomer composition essentially dictates the dispersion quality of electrode components. As illustrated in Figure 1b, there is an optimal composition achieving a highly dispersed electrode structure. As will be demonstrated later, PNCI333, with nearly identical molar content of the C and I units, exhibits the most uniformly dispersed electrode. However, in the case of PNCI324 (i.e., high I content), the adhesion to NCM is insufficient primarily due to its low carboxylic acid content, resulting in poor dispersion of NCM. Similarly, PNCI342 (i.e., high C content) fails to effectively disperse NCM and conductive carbon particles because the reduction in surface energy is not significant enough.

2.2. Effect of Binders on Adhesion and Dispersion Properties of NCM Cathodes

To investigate the effect of the PNCI# binder on the adhesion properties of NCM cathodes, a 180° adhesion test was performed on NCM cathodes prepared with PVDF and PNCI# binders (**Figure 2**a). The PNCI# cathodes exhibited significantly higher adhesion strength than the PVDF cathode. Increasing the carboxylic acid content in the PNCI# binder enhanced the adhesion strength values, presumably due to the increased hydrogen bonding between the carboxylic acid and the hydroxyl groups on the surface of NCM and the Al current collector.[44] Given that this 180° adhesion test primarily represents the weakest interfacial adhesion site where mechanical cracks or delamination occur, we additionally utilized the surface and interfacial cutting analysis system (SAICAS) to evaluate the adhesion properties of NCM cathodes within the cathode composite layer at a specific depth (see Figure S10 for the representative SAICAS profiles, Supporting Information).[52,53] As depicted in the cartoon in Figure 2b, we inserted a blade with a rake and clearance angle of 20° and 10°, respectively, to a depth of 10 μm. By horizontally moving the blade, the peeling force within the cathode was measured, providing a reliable assessment of the adhesion property inside the cathode composite layer. Interestingly, the peeling force values determined by SAICAS exhibited a different trend in adhesion strength values obtained by the 180° adhesion test. Specifically, the PNCI333 cathode showed the highest peeling force among the PNCI# cathodes despite the lower C unit content than PNCI342. It is worth noting that the peeling force is not solely determined by the hydrogen bonding between the carboxylic acid group of a binder and the surface hydroxyl group of NCM. This finding prompted us to consider other factors that significantly influence the adhesion property of the cathodes, such as the dispersion of the electrode components.

To assess the dispersion state of the NCM cathodes, EDS mapping was conducted for the cross-sectional SEM images of the NCM cathodes (Figure 2c–f). The carbon (C), fluorine (F), and nickel (Ni) maps reflect the dispersion state of the conductive carbon, binder, and NCM, respectively. The PNCI333 cathode exhibited the most compact and uniformly dispersed structure among the prepared cathodes. Specifically, the PNCI333 cathode

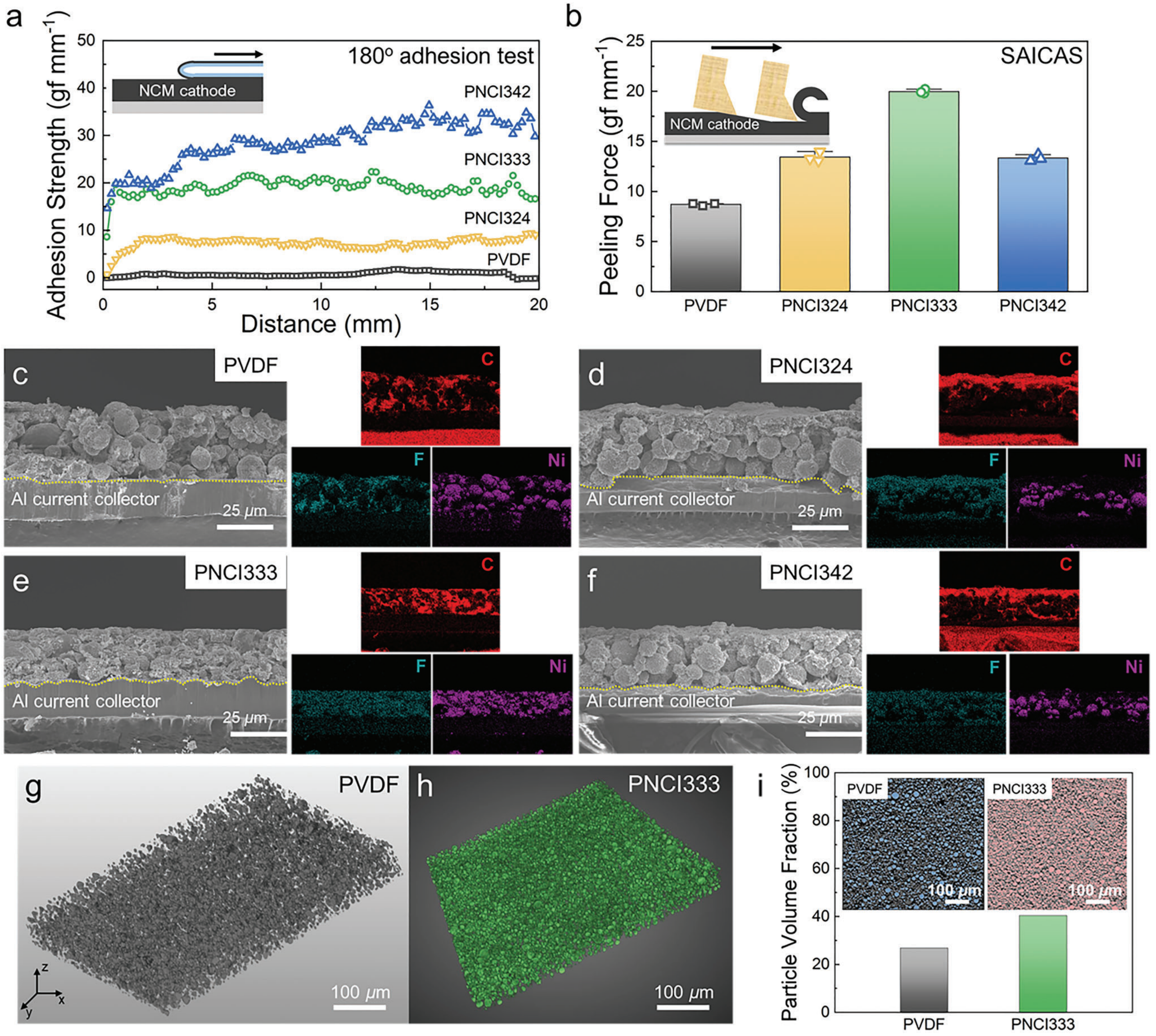

Figure 2. Adhesion and dispersion properties of NCM cathodes prepared with PVDF and PNCI# binders (NCM: Super P: binder = 90:5:5 wt%). a) 180° adhesion test profiles of the NCM cathodes with PVDF or PNCI# binder. b) Peeling force values measured by SAICAS. Cross-sectional SEM images and the corresponding EDS maps of the NCM cathodes prepared with c) PVDF, d) PNCI324, e) PNCI333, and f) PNCI342 binder. 3D XRM images of the g) PVDF and h) PNCI333 cathodes. i) Particle volume fraction of the PVDF and PNCI333 cathodes, where the inset shows cross-sectional XRM images used for the volume fraction calculations.

showed a uniform distribution of conductive carbon particles throughout the cathode layer (Figure 2e), while the PNCI324 and PNCI342 cathodes (Figure 2d,f) exhibited an accumulation of conductive carbon particles on the upper surface of the cathode layer presumably due to the hydrophobicity-driven localization (Figure S11, Supporting Information).[34,54] It is notable that the molar composition of the N, C, and I units in the PNCI# system has a significant impact on the dispersion quality of NCM cathodes. We hypothesize that the surface energy and polarity of the binders play a crucial role in determining the dispersion behavior of electrode components. The contact angle measurements of PNCI#s (Figure S12, Supporting Information) demonstrate that the PNCI# series, comprising different molar compositions of polar carboxylic acid and nonpolar perfluoroalkyl moieties, exhibit distinct surface energy and polarity characteristics (Table S2, Supporting Information). It was found that increasing the I unit reduces both the surface energy and polarity of the PNCI#s. Although the PNCI324, with the highest I unit content, exhibited the lowest surface energy among the PNCI#s, the PNCI cathode showed a poor dispersion state primarily due to inadequate adhesion toward NCM ascribed to the insufficient polarity. Conversely, the PNCI342 cathode with the lowest I unit content demonstrated reduced adhesion with conductive carbon, possibly due to excessively high polarity. Furthermore, the

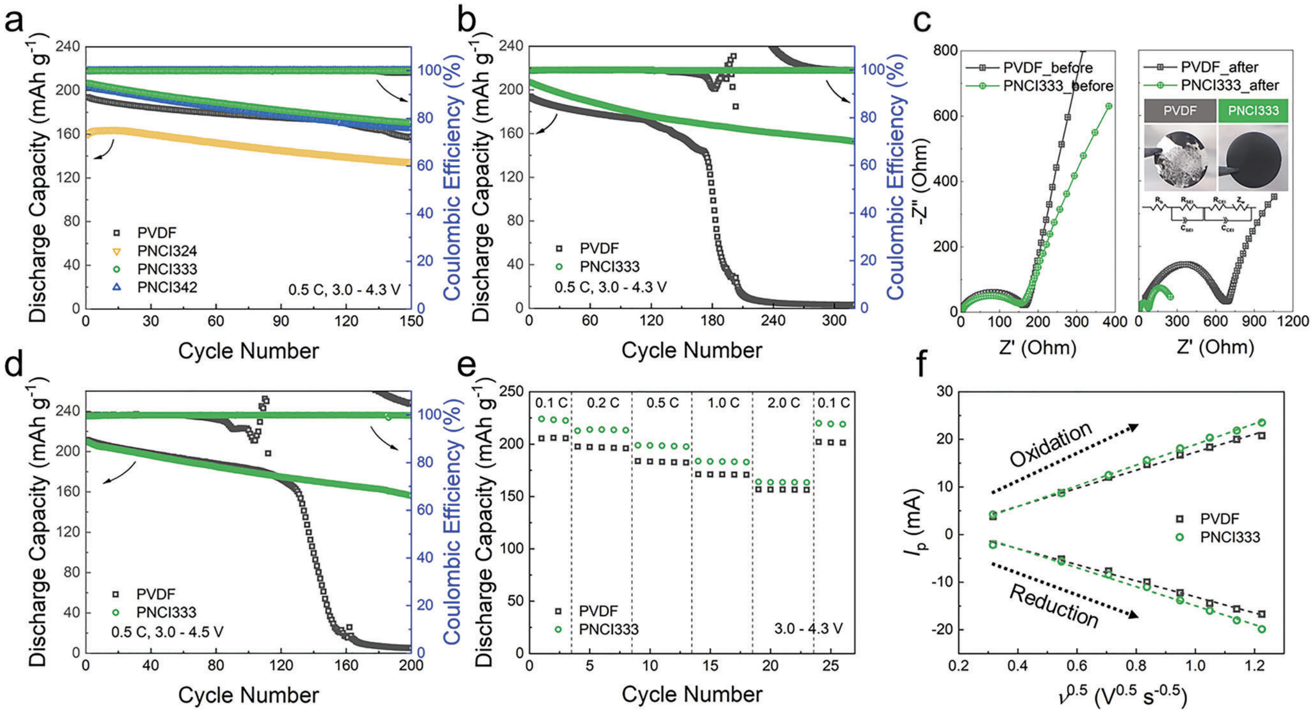

Figure 3. Cycling performance of Li/Celgard®2320/NCM811 cells prepared with PVDF and PNCI# binders (NCM811: Super P: binder = 90: 5: 5 wt%) (active material loading: 5–7 mg cm^{-2}, operation temperature: 30 °C). a) Cycling performance of the cells with PVDF and PNCI# binders cycled at 0.5 C within the voltage range of 3.0–4.3 V. b) Long-term cycling performance of the cells with PVDF and PNCI333 binder cycled at 0.5 C within the voltage range of 3.0–4.3 V. c) Nyquist plots and the equivalent circuit of the cells with PVDF and PNCI333 binder before (left) and after (right) 300 cycles, where the inset shows optical photographs of the cycled PVDF and PNCI cathodes. d) High-voltage cycling performance of the cells with PVDF and PNCI333 binder cycled at 0.5 C within the voltage range of 3.0–4.5 V. e) Rate capability of the cells with PVDF and PNCI333 binder. f) Linear plot of peak current (I_p) versus square root of potential scanning rate ($\nu^{0.5}$).

highest surface energy of PNCI342 hampers the effective dispersion of electrode components. In contrast, the PNCI333 cathode, with nearly equal molar content of the C and I units, exhibited sufficiently low surface energy with optimal polarity required for the uniform dispersion of the cathode components. The low surface energy derived from the perfluoroalkyl group in the I unit contributes to enhancing the dispersion behavior, while the optimized polarity of PNCI333 promotes interactions with both the NCM and conductive carbon. Consequently, PNCI333 acts as an effective surfactant reducing the surface tension between NCM and conductive carbon particles. To further investigate the influence of perfluoroalkyl chains on the dispersion behavior, we synthesized PNCbI333, which incorporates butyl norbornene imide (bNI) with an equivalent carbon content to the NI monomer but lacks any fluorine atoms. (Figures S13–S15, Supporting Information). The PNCbI333 cathode displayed poor dispersion quality compared to the PNCI333 cathode (Figure S16, Supporting Information), suggesting that the presence of the perfluoroalkyl chain is crucial for achieving low surface energy for the uniform dispersion of the cathode components. Furthermore, the PNCI333 cathode slurry dispersed in NMP exhibited the highest viscosity compared to the other PNCI# variants and PVDF (Figure S17, Supporting Information), which is advantageous in retaining the elastic properties of the slurry over a certain period, facilitating the uniform dispersion of the cathode components, as previously addressed by Ahn et al.[55] The 3D XRM images additionally confirmed the uniform dispersion of the PNCI333 cathode, displaying more even and compact morphology within the electrode composite layer compared to the PVDF cathode (Figure 2g,h). Moreover, the PNCI333 cathode demonstrated a significantly higher particle volume fraction (40%) compared to the PVDF cathode (27%), providing quantitative evidence for a more compact and uniform electrode structure (Figure 2i).

2.3. Roles of Binders in Determining Cycling Performance of NCM Cathodes

The cycling performance of Li/Celgard2320/NCM811 cells prepared with a series of PNCI# and PVDF binders was evaluated (**Figure 3**a). Among the PNCI# cathodes, the PNCI333 cathode, which exhibited the most uniformly dispersed cathode structure and the highest peeling force demonstrated superior cycling performance. This result highlights that the dispersibility of the binder, along with the adhesion strength and electrolyte welling resistance, is one of the important key parameters dictating the cycling performance of NCM cathodes. We speculate that the exquisite manipulation of the molar composition, which governs the overall interactions between the binder and the other cathode components as discussed earlier, plays a significant role in determining cycling performance. The inferior cycling performance of the PNCI324 cathode can be attributed to both the electrolyte swelling issue associated with PNCI324 and the non-uniform dispersion of the cathode (see Figure S18 for the electrolyte uptake values of PVDF and PNCI#s, Supporting Information). Further evidence supporting the significance of binder property was obtained by comparing the cycling performance of the PNCI333 cathode with the control PNCbI333 cathode, which lacks any perfluoroalkyl moieties (Figure S19, Supporting Information). The PNCbI333 cell delivers lower discharge capacity than the PNCI333 cell, primarily attributed to the lack of uniformly dispersed electrode structure, driven by the non-optimized surface energy and polarity of PNCbI333.

The long-term cycling stability of the PNCI333 and PVDF cell was further assessed (Figure 3b; Figure S20 for voltage-capacity profiles, Supporting Information). The PNCI333 cell retains 75% of its initial discharge capacity after 300 cycles, remarkably surpassing the PVDF cell, which experiences a dramatic capacity decay after 180 cycles. Additionally, the PNCI333 cell exhibited a higher initial Coulombic efficiency of 93.36% compared to the PVDF cell (92.17%), implying that the PNCI333 binder facilitates the formation of a stable cathode-electrolyte interphase (CEI) layer. This is primarily because the highly adhesive PNCI333 induces intimate coverage over the NCM particles, effectively passivating the NCM surface. The EIS spectra in Figure 3c further corroborate the stabilization of SEI and CEI layers enabled by the PNCI333 binder. The PNCI333 cell exhibited significantly smaller charge-transfer resistances primarily representing the SEI and CEI impedances, presented as first and second semi-circles in the Nyquist plot, compared to the PVDF cell.[56] These significantly smaller charge-transfer resistances observed in the PNCI333 cell demonstrate the effective stabilization of both SEI and CEI layers achieved through the incorporation of the PNCI333 binder.[57] Conversely, the singular semi-circle observed in the PVDF cell can be attributed to the formation of notably thick SEI and CEI layers, which substantially elevate the charge-transfer resistance at the electrode interfaces, as will be discussed later. Moreover, the optical photographs of the cycled cathodes (Figure 3c inset) and separators (Figure S21, Supporting Information) showed that the cathode composite layer of the PVDF cathode was mostly delaminated from the Al current collector, while that in the PNCI333 cell was preserved well, demonstrating again the superior adhesion strength of the PNCI333 binder. The hydrophobic polynorbornene backbone of PNCI333 that resists swelling by liquid electrolytes additionally contributes to the structural integrity of the cathode, whereas swelling-intolerant PVDF might accelerate the delamination of the cathode layer.[23]

To evaluate the high-voltage cycling stability, we increased the cut-off voltage from 4.3 to 4.5 V (Figure 3d, see Figure S22 for the voltage-capacity profiles, Supporting Information). The PNCI333 cell exhibited remarkably stable cycling over 200 cycles with 75% initial capacity retention, while the PVDF cell showed an abrupt capacity fading after 120 cycles. Additionally, the PVDF cell exhibited a large fluctuation in Coulombic efficiencies prior to the capacity decay, presumably due to irreversible capacity loss caused by unstable CEI formation. Furthermore, as corroborated by the LSV and CV results (Figure S23, Supporting Information), the PNCI333 binder demonstrated a wider electrochemical stability window up to 4.5 V compared to PVDF (4.4 V). A slight increase in current observed above 4.0 V in the LSV of the PNCI333 binder is possibly attributed to the oxidation of the double bond in the norbornene backbone.[58] However, the CV curves of the PNCI333 electrode demonstrated the absence of further oxidative side reactions during subsequent cycles (Figure S23c, Supporting Information). Figure 3e demonstrates the rate capabilities of the cells cycled at various C-rates. The PNCI333 cell exhibited superior rate capability over the PVDF cell, which can be attributable to the uniformly dispersed electrode structure enabling fast electron transport through the well-dispersed conductive carbon.[32,59] Furthermore, stable CEI layer formation also leads to efficient electrochemical reaction kinetics, as further demonstrated by determining the Li-ion diffusivities by the Randles-Sevcik equation (Figure 3f; Figure S24, Supporting Information).[60] The anodic and cathodic Li-ion diffusivities of the PNCI333 cell were found to be higher than those of the PVDF cell by 1.15 and 1.18 times, respectively, demonstrating the efficient electrochemical kinetics enabled by adopting the PNCI333 binder.

2.4. Post-Mortem Analysis of the Cycled NCM Cathodes and Li Metal

To probe the physicochemical state of the cycled NCM cathodes, a series of post-mortem analyses were conducted. **Figure 4**a presents the scanning transmission electron microscopy (STEM) images with fast Fourier transform (FFT) patterns of the cycled NCM cathodes prepared with PVDF and PNCI333 binder. The surface of NCM in the PVDF cathode exhibited a thick NiO-type rock-salt phase ($Fm\bar{3}m$) with the thickness of 40–50 nm, primarily due to cation mixing (see Figure S25 for the low-magnification TEM image, Supporting Information).[61] The amorphous phase surrounding the NCM particle originated from the thick CEI layer formed as a result of electrolyte decomposition.[62] In contrast, the PNCI333 cathode remarkably preserved the electrochemically active layered phase ($R\bar{3}m$) of NCM, with a very thin (2–3 nm) rock-salt phase at the NCM surface.[61] This observation highlights that the effective wrapping of NCM particles by the highly adhesive PNCI333 binder stabilizes the NCM surface through TM ion chelation, thereby mitigating cation mixing and TM dissolution during cycling. Consequently, the NCM particle in the PNCI333 cathode exhibited significantly fewer microcracks compared to that in the PVDF cathode (Figure 4b), primarily because the internal strains derived from the cation mixing were considerably alleviated by the PNCI333 binder.[22] Furthermore, the suppressed phase transition and cation mixing of NCM lead to minimizing electrolyte decomposition, thereby constructing a thin and compact CEI layer on the NCM surface.[63] As corroborated by the top-surface SEM images of the cycled NCM cathodes (Figure 4c), the morphologies of the NCM particles were retained well in the PNCI333 cathode, while the surface and individual NCM particles of the PVDF cathode were covered by relatively thick CEI layers (Figure S26, Supporting Information). The stabilization of the CEI layer is also associated with the regulation of TM ion crossover from the NCM cathode to the anode side.[22] The PNCI333 binder can chelate TM ions through the coordination with carboxylic acid moieties, leading to significant suppression of TM ion dissolution and

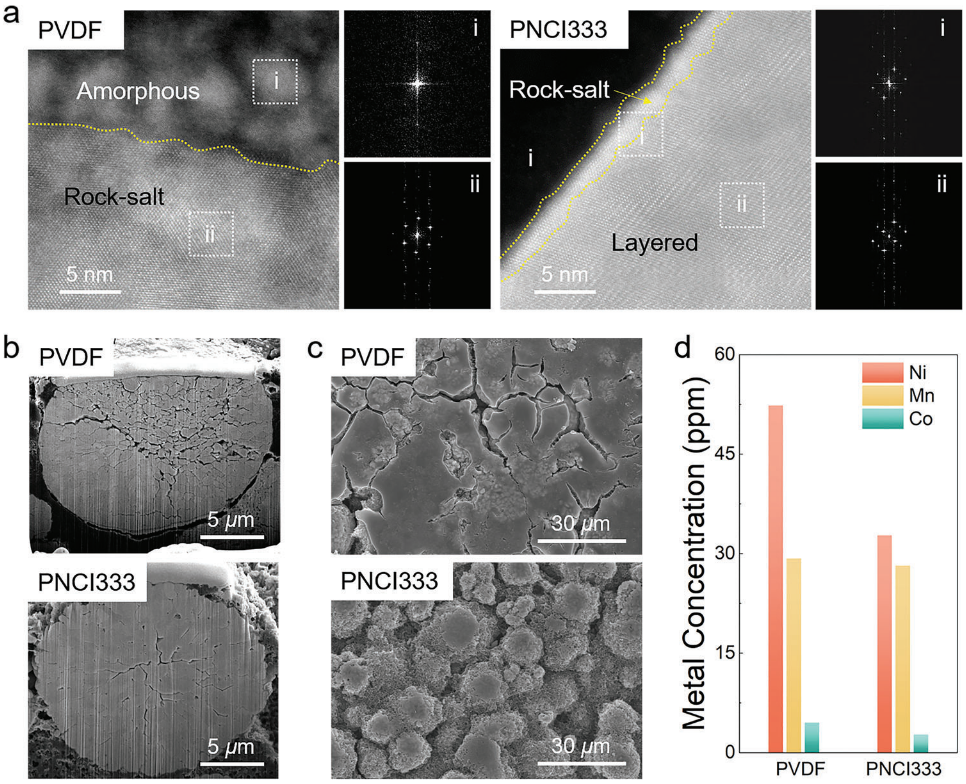

Figure 4. Post-mortem analysis of the NCM cathodes prepared with PVDF and PNCl333 binder after 300 cycles under 0.5 C at 30 °C within the voltage range of 3.0–4.3 V. a) STEM images with fast Fourier transform (FFT) patterns, b) cross-sectional FIB-SEM images, and c) top-surface SEM images of the PVDF and PNCl333 cathode. d) Concentration of Ni, Co, and Mn ions deposited on the surface of Li metal anode of the PVDF and PNCl333 cell determined by ICP-MS.

subsequent reduction in interfacial side reactions.[22,23] To quantitatively assess the TM ion-chelating capability of PNCl333, the TM ion concentration deposited on the Li metal surface was determined using inductively coupled plasma-mass spectrometry (ICP-MS) analysis (Figure 4d). The results revealed substantially lower TM ion concentrations, particularly Ni ions, on the Li metal surface in the PNCl333 cell compared to the PVDF cell, indicating that PNCl333 effectively chelates TM ions, likely through the formation of TM ion-carboxylic acid complexes.[23,64] The inhibition of TM ion crossover further contributes to the stabilization of the Li metal anode, as verified by the SEM images of the Li metal (Figure S27, Supporting Information). The Li metal in the PNCl333 cell exhibited a significantly thin passivating layer on the surface primarily consisting of the solid electrolyte interphase (SEI) layer, Li dendrites, and dead Li, while that in the PVDF cell shows a relatively thick and irregular passivating layer. These results highlight the significant role of PNCl333 binder in mitigating interfacial side reactions in both the NCM cathode and the Li metal anode.[65]

2.5. Post-Mortem In-Depth Characterizations of the CEI Layers on the Cycled NCM Cathodes

To probe the quantitative chemical composition and spatial distribution of CEI layers on the cycled NCM cathodes, in-depth X-ray photoelectron spectroscopy (XPS) and time-of-flight secondary ion mass spectrometry (TOF-SIMS) analyses were conducted (**Figure 5**). Figure 5a presents the XPS depth profiling obtained by Ar-ion etching through the CEI layer of the PVDF and PNCl333 cathodes. Notably, the PNCl333 cathode exhibited a smaller amount of O and Ni atoms in the CEI layer compared to the PVDF cathode. This is likely due to the effective suppression of electrolyte decomposition and TM dissolution facilitated by the highly adhesive PNCl333 binder.[22] As shown in the representative deconvoluted C 1*s* spectra (Figure 5b,c), a significantly larger quantity of C–O containing species is observed in the PVDF cathode compared to the PNCl333 cathode, suggesting that the decomposition of carbonate electrolytes occurs at a faster rate in the PVDF cathode than in the PNCl333 cathode.[10,11] In the F 1*s* spectra, the PVDF cathode shows a strong LiF signal at 685.7 eV, possibly originating from the decomposition of $LiPF_6$ salt in the electrolytes, while that in the PNCl333 cathode is relatively weak.[66,67] The formation of LiF on the cathode surface can impede electrochemical reaction kinetics primarily due to its highly resistive nature, consequently resulting in capacity fading during cycling.[68] Additionally, since LiF formation is typically accompanied by the generation of hydrofluoric acid (HF),[69] the PVDF cathode may experience accelerated TM ion dissolution, further deteriorating the cycling performance. In the Ni 2*p* spectra, the Ni $2p_{3/2}$ regime at ≈856 eV is deconvoluted into two distinct valence states of Ni; Ni^{2+} and Ni^{3+} located at 854.7 and 857.5 eV, respectively.[70] The PNCl333 cathode exhibited a significantly lower Ni^{2+}/Ni^{3+} ratio

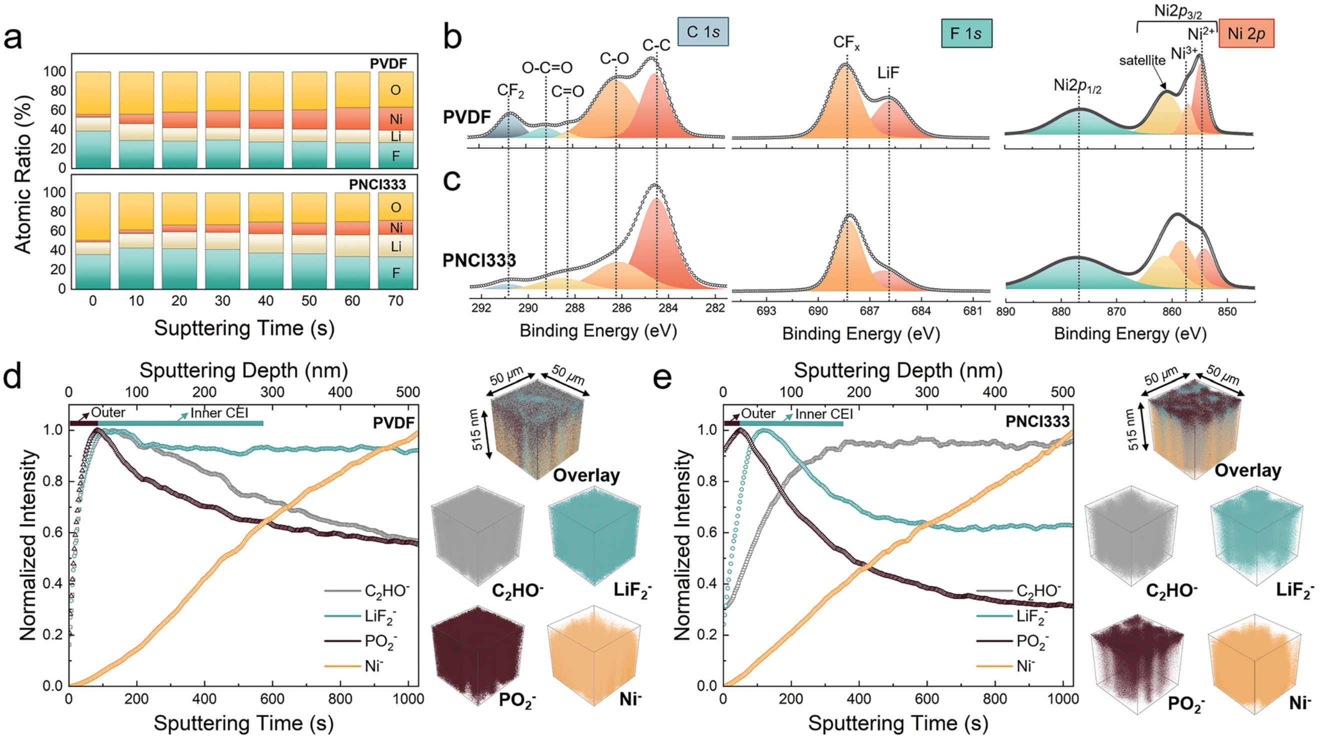

Figure 5. Post-mortem in-depth characterizations of the CEI layers on the cycled NCM cathodes prepared with PVDF and PNCI333 binder. a) In-depth XPS profiling of the atomic ratio of the PVDF and PNCI333 cathode. Representative deconvoluted C 1*s*, F 1*s*, and Ni 2*p* XPS spectra of the b) PVDF and c) PNCI333 cathode. Normalized TOF-SIMS depth profiles of the d) PVDF and e) PNCI333 cathode with 3D maps of the selected species and overlayed images.

compared to the PVDF cathode, indicating that cation mixing between Li$^+$ and Ni^{2+} was effectively inhibited in the PNCI333 cathode.[69,70] This inhibition is particularly beneficial for preserving the layered NCM structure, contributing to improved cycling performance.

To further investigate the spatial distribution of the CEI components and the thickness of the passivating layer on the cycled NCM cathodes, TOF-SIMS analysis was carried out. Figure 5d,e present TOF-SIMS depth profiles and corresponding 3D maps of CEI species of interest on the PVDF and PNCI333 cathodes after 300 cycles. Note that the C_2HO^- species detected from the PVDF cathode derive from the decomposition of carbonate electrolytes, while those in the PNCI333 cathode additionally include the ionized PNCI333 binder. The inorganic LiF_2^- and PO_2^- species originate from the decomposed FEC additive and LiPF$_6$ salt in the electrolytes,[22,71] where a portion of LiF_2^- is possibly generated by ionization of PVDF and PNCI333 binder. The scale bar in the depth profile represents the CEI layer thickness, where the dark brown and turquoise colors indicate the outer and inner CEI layers, respectively. The outer CEI thickness was determined by locating the maximum point of PO_2^-, as the outer CEI is predominantly composed of LiPF$_6$ decomposition species.[72,73] In the PVDF cathode profile, the inner CEI thickness was identified by the intersection point between PO_2^- and Ni$^-$, where the intensity of the bulk Ni phase is stronger than that of the CEI species.[74] However, for the PNCI333 cathode profile, the intersection point of PO_2^- and Ni$^-$ was not used to determine the inner CEI thickness, because the C_2HO^- intensity already reaches its maximum equilibrium point prior to the intersection point. While the C_2HO^- intensity in the PVDF cathode profile decreases upon sputtering, that in the PNCI333 cathode continuously increases and reaches a maximum point, presumably due to the ionization of the PNCI333 binder after passing through the CEI layer. Thus, the inner CEI thickness of the PNCI333 cathode was estimated by identifying the point at which the C_2HO^- intensity reaches its maximum value. Our findings reveal that both the outer and inner CEI layers of the PNCI333 cathode are significantly thinner than those of the PVDF cathode, with the total thickness of the PNCI333 cathode being only 62% of that observed in the PVDF cathode. Specifically, the inner CEI layer of the PVDF cathode accounts for 85% of the overall CEI thickness, indicating the formation of an organic-rich CEI layer mainly composed of C_2HO^- and LiF_2^-. In contrast, the PNCI333 cathode exhibited a considerably reduced thickness in the inner CEI layer, suggesting that the decomposition of the organic compound was significantly mitigated through the stabilization of reactive TM ions, enabled by the PNCI333 binder. Moreover, the dehydrofluorination-resistant perfluoroalkyl chain of PNCI333 inhibits HF formation, effectively suppressing the dissolution of TM ions and promoting CEI layer stability.[66] Indeed, the LiF_2^- and PO_2^- intensities of the PVDF cathode strongly persisted upon sputtering, primarily due to LiF formation, while that of the PNCI cathode was decreased after 100 s, which is consistent with the XPS results. The 3D TOF-SIMS maps of the cathodes also show a good correlation with the aforementioned findings.

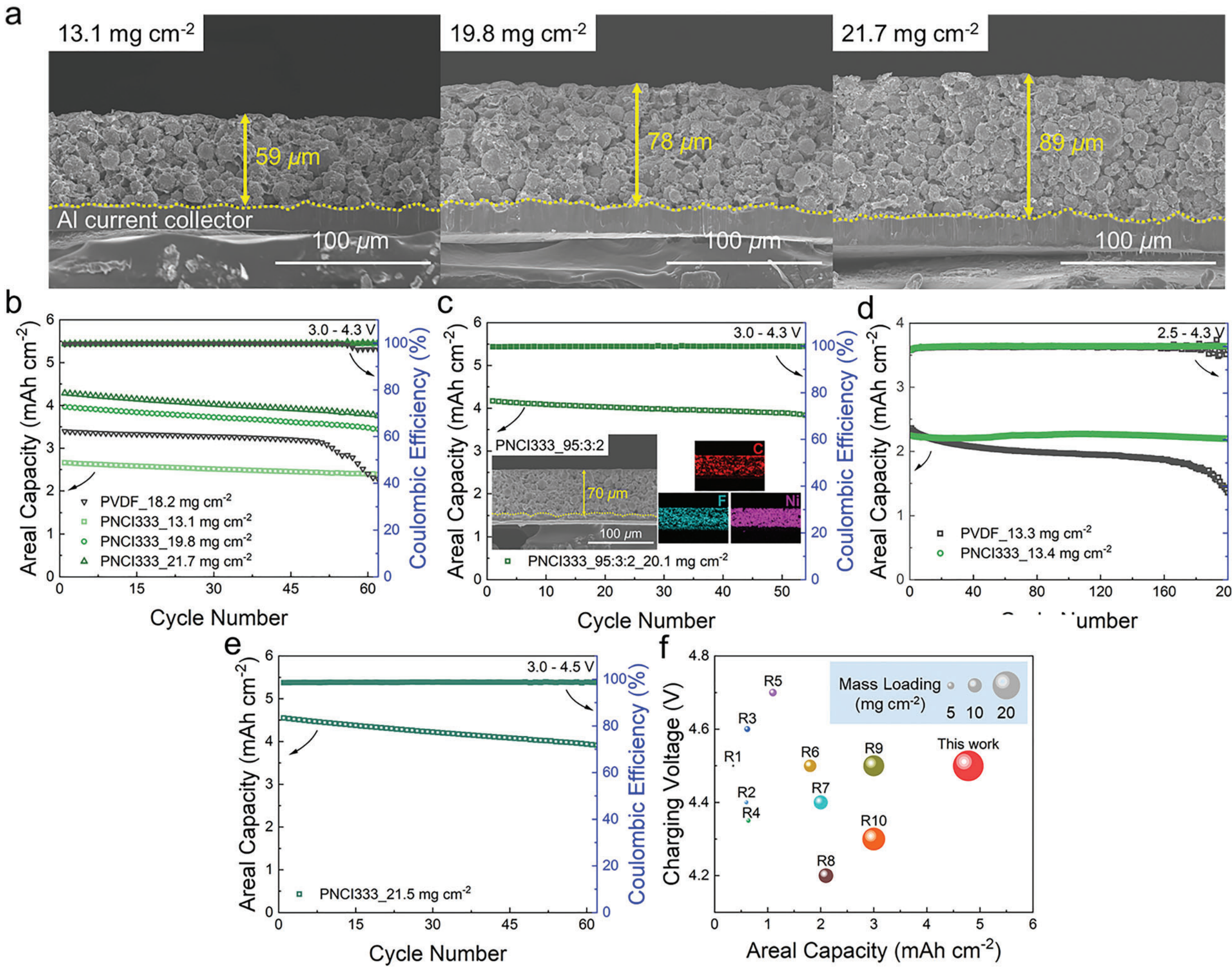

Figure 6. Cycling performance of high-loading PNCI333 cathode cycled under 0.2 C-rate at 30 °C, where the NCM cathode was prepared with the composition of NCM811: Super P: binder = 90: 5: 5 (wt%) otherwise denoted. a) Cross-sectional SEM images of the PNCI333 cathode with different areal mass loading. b) Cycling performance of the PVDF and PNCI333 cathode with different areal mass loading. c) Cycling performance of the high-loading PNCI333 cathode with lower binder content (2 wt%) d) Cycling performance of graphite/Celgard®2320/ NCM811 full cells under 0.5 C-rate (N/P ratio < 1.2) e) Cycling performance of the PNCI333 cathode in the cut-off voltage range of 3.0–4.5 V. f) Comparison of areal capacity, mass loading, and charging voltage of the PNCI333 cathode compared with other works.

2.6. High-Loading Cell Demonstration

The high-loading of the active material is one of the essential challenges for high-energy-density batteries. We speculate the PNCI333 binder, with its robust adhesion and ability to create an exceptionally uniform cathode structure, is promising for the highly NCM-loaded cathodes. Thus, high-loading PNCI333 cathodes were prepared with areal mass loadings of 13.1, 19.8, and 21.7 mg cm^{-2}, corresponding to electrode thicknesses of 59, 78, and 89 *μm*, respectively. **Figure 6**a shows the cross-sectional SEM images of the high-loading PNCI333 cathodes; a uniform and compact electrode was achieved even under the high-loading condition. In contrast, the high-loading PVDF cathode, with an areal mass loading of 18.2 mg cm^{-2}, exhibited a non-uniform structure and loose contact with the current collector (Figure S28, Supporting Information). This comparison highlights the superior performance of the PNCI333 binder in maintaining a uniform and well-connected electrode structure, even at high-loading conditions, ensuring efficient charge transport and improved electrochemical performance.[23] As a result, the PNCI333 cathodes demonstrated stable cycling performance with the highest areal capacity exceeding 4.5 mAh cm^{-2}, while the high-loading PVDF cathode failed to maintain its capacity after 55 cycles (Figure 6b). The full utilization of the theoretical capacity of NCM811 was further confirmed by converting the areal capacity into specific capacity (mAh g^{-1}), where all the high-loading cells delivered a specific capacity that closely matches the theoretical capacity of NCM811, which is ≈200 mAh g^{-1} (Figure S29, Supporting Information). Furthermore, a high-loading PNCI333 cathode (≈20 mg cm^{-2}) prepared with a reduced binder content of 2 wt% exhibited a uniform and compact structure, as demonstrated by cross-sectional SEM images of the cathode in the inset of Figure 6c. This result indicates the capability of the PNCI333 binder to sustain a consistent electrode structure even with a lower amount of binder, primarily attributable to its highly adhesive and dispersive properties.[23,25,75] Notably, this cathode showed stable cycling performance, delivering an areal capacity of over 4 mAh cm^{-2}, highlighting the effectiveness of the PNCI333 binder in constructing high-loading cathodes (Figure 6c). Additionally, the superior binder performance of PNCI333 demonstrated remarkably stable full cell performance, retaining an areal capacity of 2.2 mAh cm^{-2} for 200 cycles, significantly surpassing those of the PVDF cell (1.4 mAh cm^{-2} for 200 cycles) (Figure 6d). Furthermore, the high-loading PNCI333 cathode exhibited excellent cycling performance even within the voltage range of 3.0–4.5 V (Figure 6e) presumably due to the presence of oxidative stability of the polynorbornene backbone with electron-withdrawing perfluoroalkyl chains.[76] All the advantageous properties exhibited by the PNCI333 binder allow for the construction of cathodes capable of accommodating larger quantities of active material and withstanding high-voltage conditions. As summarized in Figure 6f and Table S3 (Supporting Information), the high-loading PNCI333 cathode exhibited superior cycling performance compared to numerous previously reported studies, surpassing them in terms of areal mass loading, areal capacity, and charging voltage.

3. Conclusion

We have demonstrated that polynorbornene-based binders with delicately optimized properties effectively alleviate the degradation issues of Ni-rich layered oxide cathodes. By systematically modulating the surface energy and polarity through variations in functionalities and compositions of monomeric units, we have explored the significant roles of binder properties in determining the adhesion and dispersion state of NCM cathodes. The PNCI333 binder, with its optimized adhesion strength, surface energy, and polarity, facilitates the formation of a highly uniform electrode structure. The highly adhesive PNCI333 binder effectively stabilizes the NCM surface through TM ion chelation, thereby mitigating phase transition and cation mixing of NCM. Consequently, the PNCI333 binder enables the construction of a thin and compact CEI layer on the NCM surface by minimizing uncontrolled electrolyte decomposition and TM ion dissolution, as revealed by post-mortem analyses using STEM, XPS, and TOF-SIMS. The advantageous electrochemical properties of the PNCI333 binder allow for achieving high-performance NCM cathodes capable of accommodating high areal mass loading of the active material and tolerating high-voltage conditions. This study highlights the significant role of polymer binders in accessing uniformly structured high-performance NCM cathodes. The findings of this study emphasize the importance of striking a balance between functionalities and composition in binder system to achieve high-performance NCM cathodes, and further provide fresh insights into the rational design of multifunctional binders for high-Ni cathode materials.

4. Experimental Section

Materials: 2–Norbornene, *cis*–5–norbornene–*endo*–2,3–dicarboxylic anhydride, 2,2,3,3,4,4,4–heptafluorobutylamine, sodium acetate, acetic anhydride, Grubbs Catalyst 3rd Generation (G3, M300), *n*-butylamine, and triethylamine (TEA) were purchased from Sigma–Aldrich. Poly(vinylidene fluoride) (PVDF, average M_w ≈352,000 g mol^{-1}) was purchased from PolyK Technologies (USA). $LiNi_{0.8}Co_{0.1}Mn_{0.1}O_2$ (NCM811) was purchased from COSMO AM&T CO., LTD. (Korea). 1.2 M lithium hexafluorophosphate ($LiPF_6$) in a mixture of ethylene carbonate (EC) and dimethyl carbonate (DMC) (3:7 vol%) with 2 wt% of vinyl carbonate (VC) and 10 wt% of fluoroethylene carbonate (FEC) was purchased from Welcos Co., Ltd (Korea). A trilayer polypropylene/polyethylene/polypropylene (PP/PE/PP, Celgard2320, thickness: 25 μm) laminated film was used as a separator for electrochemical analyses. All other chemicals and solvents were purchased from reliable commercial sources and used as received.

Preparation of Cis-5-Norbornene-exo-2,3-Dicarboxylic Anhydride (NA): *Cis*-5-Norbornene-*endo*-2,3-dicarboxylic anhydride (50 g) was dissolved in 1,2-dichlorobenzene (100 mL) and the solution was stirred at 185 °C for 24 h with a reflux condenser.[77] The resulting solution was cooled down to room temperature and the crystallized product was collected by filtration. The obtained crystalline solid (25 g) was dissolved in benzene (25 mL) and heated to reflux for 2 h and recrystallized at room temperature. After the recrystallization in benzene three times, NA was obtained as a white crystalline solid with a 20% yield. ^1H NMR (400 MHz, $CDCl_3$): δ [ppm] = 6.34 ($CH=CH$, 2H), 3.46 ($CH\text{-}CH\text{-}CH$, 2H), 3.01 ($CO\text{-}CH$, 2H), 1.67 and 1.45 ($CH\text{-}CH_2\text{-}CH$, 2H).

Synthesis of Heptafluorobutyl Norbornene Amic Acid (NAA): NA (2.0 g, 12 mmol) and 2,2,3,3,4,4,4–heptafluorobutylamine (2.7 g, 13 mmol) were dissolved in toluene (40 mL) and the solution was stirred at 100 °C for 2 h with a reflux condenser. The resulting white precipitate was collected by filtration, washed several times with toluene, dried under vacuum, and stored at room temperature. ^1H NMR (400 MHz, DMSO–d_6): δ [ppm] = 11.89 ($COOH$, 1H), 8.58 ($CONH$, 1H), 6.22 ($CH=CH$, 2H), 4.02 and 3.85 ($NH\text{-}CH_2\text{-}CF_2$, 2H), 2.95 and 2.72 ($CH\text{-}CH\text{-}CH$, 2H), 2.57 and 2.33 ($CO\text{-}CH$, 2H), 2.16 and 1.25 ($CH\text{-}CH_2\text{-}CH$, 2H).

Synthesis of Heptafluorobutyl Norbornene Imide (NI): NAA (4.0 g, 11 mmol) and sodium acetate (0.52 g 6.3 mmol) were added to acetic anhydride (19 mL) and the mixture was stirred at 130 °C for 4 h with a reflux condenser. The resulting solution was poured into DI water and vigorously stirred to precipitate NI as a white powder. The precipitate was collected by filtration and dissolved in acetone to further precipitate in DI water two times. After drying under vacuum at 60 °C, NI was obtained as a white powder with 90% yield. ^1H NMR (400 MHz, DMSO–d_6): δ [ppm] = 6.33 ($CH=CH$, 2H), 4.24 ($CH_2\text{-}CF_2$, 2H), 3.16 ($CH\text{-}CH\text{-}CH$, 2H), 2.84 ($CO\text{-}CH$, 2H), 1.39 and 1.19 ($CH\text{-}CH_2\text{-}CH$, 2H).

Synthesis of Butyl Norbornene Imide (bNI): NA (2.0 g, 12 mmol), *n*-butylamine (0.98 g, 13 mmol), and TEA (0.12 g, 1.2 mmol) were dissolved in toluene (20 mL) and the solution was stirred at 110 °C for 24 h with a reflux condenser. After the reaction, toluene was removed by a rotary evaporator, and the crude solution was diluted with MC (100 mL) and extracted three times: once with 100 mL of 2% (v/v) HCl and twice with 100 mL of brine solution. The organic layer was dried over anhydrous magnesium sulfate and filtered. After drying under vacuum at room temperature, bNI was obtained as a transparent and viscous liquid. ^1H NMR (400 MHz, $CDCl_3$): δ [ppm] = 6.28 ($CH=CH$, 2H), 3.47 ($N\text{-}CH_2\text{-}CH_2$, 2H), 3.27 ($CH\text{-}CH\text{-}CH$, 2H) and 2.67 ($CO\text{-}CH$, 2H), 1.53, 1.32, 1.23, and 0.93 ($CH\text{-}CH_2\text{-}CH$ and $N\text{-}CH_2\text{-}CH_2\text{-}CH_2\text{-}CH_3$, 9H).

Synthesis of Poly(Norbornene–Co–Norbornene Anhyride–Co–Norbornene Imide) (PNAI): A mixture of N, NA, and NI in methylene chloride (total monomer concentration, 0.4 M) was added to a Schlenk flask equipped with a magnetic stirring bar. The solution was deoxygenated three times by freeze-pump-thaw cycles, and a predetermined amount of Grubbs Catalyst 3rd Generation (G3) stock solution was added to the solution ($[M]_0/[G]_0$ = 1800–2200). The resultant solution was stirred at 0 °C for 1 h and quenched with 0.1 mL of ethyl vinyl ether. The obtained crude solution was precipitated into methanol and the polymer was collected by filtration. The polymer was further dried under vacuum at room temperature (yield, 75%).

Synthesis of Poly(Norbornene–Co–Norbornene Dicarboxylic Acid–Co–Norbornene Imide) (PNCI):: PNAI (0.3 g) was dissolved in dimethyl sulfoxide (18 mL) and the excess amount of DI water (0.3 mL) was added to the solution. The solution was stirred at 80 °C for 24 h and the crude solution was precipitated into diethyl ether. After being dried under a dynamic vacuum condition at 60 °C, PNCI was obtained as a brown solid with a 99% yield.

Synthesis of Poly(Norbornene–Co–Norbornene Anhyride–Co–Butyl Norbornene Imide) (PNAbI): A mixture of N, NA, and bNI in methylene chloride (total monomer concentration, 1.0 M) was added to a Schlenk flask equipped with a magnetic stirring bar. The solution was deoxygenated three times by freeze-pump-thaw cycles and a predetermined amount of Grubbs Catalyst 3rd Generation (G3) stock solution was added to the solution ($[M]_0/[G]_0 = 2530$). The resultant solution was stirred at 0 °C for 1 h and quenched with 0.1 mL of ethyl vinyl ether. The obtained crude solution was precipitated into methanol and the polymer was collected by filtration. The polymer was further dried under vacuum at room temperature (yield, 75%).

Synthesis of Poly(Norbornene–Co–Norbornene Dicarboxylic Acid–Co–Butyl Norbornene Imide) (PNCbI): PNAI (0.15 g) was dissolved in dimethyl sulfoxide (9.0 mL) and the excess amount of DI water (0.15 mL) was added to the solution. The solution was stirred at 80 °C for 24 h and the crude solution was precipitated into diethyl ether. After being dried under a dynamic vacuum condition at 60 °C, PNCbI was obtained as a brown solid with a 99% yield.

Preparation of NCM811 Cathodes: $LiNi_{0.8}Co_{0.1}Mn_{0.1}O_2$ (NCM811) (90 wt%) was used as a cathode active material and dispersed in NMP with Super P (5 wt%) and binder (5 wt%) using a Thinky mixer. The resultant slurry was uniformly cast onto an aluminum (Al) current collector using a doctor blade, followed by drying under a dynamic vacuum condition at 60 °C to remove the residual NMP. The dried electrode was roll-pressed at room temperature, resulting in a thickness reduction of 20% (80% of its original thickness). The mass loading of the active materials in the NCM cathode was approximately in the range of 5.0–7.0 mg cm^{-2} and 15–25 mg cm^{-2} for low–loading and high–loading cathodes, respectively.

Preparation of Graphite Anodes: Graphite (LG Chem.) (90 wt%) was used as an anode active material and dispersed in NMP with Super P (5 wt%) and PVDF (5 wt%) using a Thinky mixer. The resultant slurry was cast onto a copper current collector using a doctor blade, followed by vacuum drying at 80 °C to remove the residual NMP. The dried electrode was roll-pressed at 80 °C resulting in a thickness reduction of 20% (80% of its original thickness). The mass loading of the active material in the graphite anode was ≈15.0 mg cm^{-2}.

Electrochemical Characterizations: Charge/discharge cycling test of Li/Celgard2320/NCM811 half-cell was conducted using a 2032 coin cell at a cut-off voltage range of 3.0–4.3 V (vs. Li/Li$^+$) at 30 °C, where 1 C corresponds to a current density of 200 mA g^{-1}. For the high-voltage cycling test, the cut–off voltage range was set as 3.0–4.5 V (vs. Li/Li$^+$). Charge/discharge cycling test of graphite/Celgard2320/NCM811 full cell was conducted using a 2032 coin cell at a cut-off voltage range of 2.5–4.3 V (vs. Li/Li$^+$) at 30 °C, where 1 C corresponds to a current density of 200 mA g^{-1}. 1 M $LiPF_6$ in EC:DMC (3:7 vol%) with 2 wt% VC and 10 wt% FEC (100 μL) was used as a liquid electrolyte, and all the cell components were assembled in an argon-filled glove box ($O_2 < 0.1$ ppm, $H_2O < 0.1$ ppm). Electrochemical impedance spectroscopy (EIS) was performed using a VMP3 multi-channel potentiostat (Biologic, France) in a frequency range from 0.1 to 100 MHz with 10 mV of amplitude at room temperature. Cyclic voltammetry (CV) was performed using a VMP3 multi-channel potentiostat (Biologic, France) in a voltage range of 3.0–4.7 V (vs. Li/Li$^+$) at a scan rate of 0.1–1.5 mV s^{-1}. Linear sweep voltammetry (LSV) was performed using a VMP3 multi-channel potentiostat (Biologic, France) in a voltage range of 3.0–7.0 V (vs. Li/Li$^+$) at a scan rate of 1.0 mV s^{-1}.

Instrumentation and Characterization Techniques: ^{1}H NMR spectra were recorded on an Ascend 400 spectrometer (400 MHz) using $CDCl_3$ with tetramethylsilane (TMS) reference (Sigma–Aldrich) and DMSO-d_6 (Sigma–Aldrich) as solvents at room temperature. Inverse-gated ^{13}C NMR spectra were recorded on an Avance600 spectrometer (600 MHz) using DMSO-d_6 (Sigma–Aldrich) as a solvent at room temperature. Molar mass and dispersity ($Đ$) were determined by size exclusive chromatography (SEC) using the Ultimate 3000 HPLC system (Thermo Fisher Scientific Inc., USA). HPLC grade THF (J. T. Baker) was used as an eluent. The glass transition temperatures of the polymers were examined by differential scanning calorimetry (DSC) using TA Instruments DSC25 under a nitrogen atmosphere. The tensile tests were conducted using the Lloyd-LS1 universal tensile machine (Lloyd, UK) with a cross-head speed of 5 mm min^{-1}. The polymer films were cut into dog-bone-shaped specimens using the ASTM standard D638-M (type V specimens), and at least five measurements were performed for each sample to determine the reliable average values. The 180° adhesion tests were carried out using a Lloyd-LS1 with a cross-head speed of 10 mm min^{-1}. The 3 M double-sided tape was attached to the electrode samples with a dimension of 1.2 × 2.0 cm^2 using a rubber roller (diameter: 95 mm, width: 45 mm, weight: 2.0 kg) to ensure consistent pressure through the experiments. The adhesion strength was recorded upon peeling at a 180° angle. The peeling force of the cathode at 10 μm depth was determined by surface and interfacial cutting analysis system (SAICAS) using the SAICAS EN-EX (Daipla Wintes Co., Ltd., Japan). A blade (width: 1 mm) fixed with a shear angle of 45°, rake angle of 20°, and clearance angle of 10° moved with a horizontal velocity of 5 μm s^{-1} for 200 s. The peeling force was determined by the following Equation (1):

$$P\ \left(\mathrm{kNm^{-1}}\right) = F_{h,avg}\ (N)\ /w\ (\mathrm{mm}) \tag{1}$$

where P is the peeling force, $F_{\mathrm{h,\ avg}}$ is the average value of horizontal force after peeling, and w is the width of the blade. The viscosity of electrode slurry was determined using a Discovery Hybrid Rheometer (DHR-2, TA Instruments, USA), equipped with a 40 mm parallel plate geometry with a loading gap of 300–700 μm depending on the amount of slurry loading. The shear rate sweep experiments were performed in the range of 0.1 to 100 s^{-1}. The electrolyte uptake value was calculated by the following Equation (2):

$$\text{Electrolyte uptake }(\%) = \left(W_{\mathrm{wet}} - W_{\mathrm{dry}}\right)/W_{\mathrm{dry}} \times 100 \tag{2}$$

where W_{dry} and W_{wet} are the weights before and after immersion in liquid electrolyte, respectively. X-ray photoelectron spectroscopy (XPS) was performed using a PHI 5000 VersaProbe (ULVAC PHI, Japan) with a monochromatized Al Kα as a radiation source. A survey spectrum was collected over a range of 0–1400 eV, followed by high-resolution narrow scans of C1s, O1s, F1s, Li1s, and Ni2p regions. Depth profiles were collected using an Ar$^+$ sputter source with a sputter rate of 0.5 nm s^{-1}. Scanning electron microscopy (SEM) was performed on a Regulus 8230–Oxford EDS (Hitachi Inc., Tokyo, Japan) at an accelerating voltage of 10 kV. SEM specimens were prepared by washing with dimethyl carbonate (DMC) followed by vacuum drying at room temperature in an Argon-filled glove box. A focused ion beam (FIB; Helios NanoLab600, FEI, US) was used to prepare transmission electron microscopy (TEM) samples. The scanning TEM (STEM) was performed on a Titan TM 80–300 (FEI, Netherlands). Time-of-flight secondary ion mass spectrometry (TOF-SIMS) was performed using a TOFSIMS.5 (ION-TOF, Germany) with a raster size of 50 × 50 μm^2. A Bi$^+$ beam (30 keV, 1 pA) was used to analyze the depth profile and a Cs$^+$ beam (3 keV, 20 nA) was used to sputter the electrodes with a sputtering rate of 0.5 nm s^{-1}. Inductively coupled plasma mass spectrometry (ICP-MS) was conducted using an iCAP RQ (Thermo Scientific, USA). Cycled Li metal anodes were immersed in fresh DMC for 24 h in an argon-filled glove box prior to ICP-MS measurement. After removing DMC by vacuum, the amount of dissolved TM ions was determined by ICP-MS. 3D X-ray microscopy (XRM) was performed using a Xradia 620 Versa with a spatial resolution of 0.6 μm.

Supporting Information

Supporting Information is available from the Wiley Online Library or from the author.

Acknowledgements

This work was supported by the New Faculty Startup Fund from Seoul National University. This work was also supported by the institutional program of the Korea Institute of Science and Technology (KIST) (No. 2E32581), the National Research Foundation of Korea (NRF) grant funded by the Korea government (MSIT) (No.2020M3H4A3081889 and RS-2023-00209631), and the Technology Innovation Program (or Industrial Strategic Technology Development Program-Development of wide width Li-foil extruder and rolling mill for next-generation lithium batteries) (No.20016018) funded by the Ministry of Trade, Industry & Energy (MOTIE, Korea).

Conflict of Interest

The authors declare no conflict of interest.

Data Availability Statement

The data that support the findings of this study are available on request from the corresponding author upon reasonable request.

Keywords

high-nickel cathode materials, lithium-ion batteries, polymer binders, ring-opening metathesis polymerization, uniform electrode dispersion

Received: September 25, 2023
Revised: October 7, 2023
Published online:

---

[1] W. He, W. Guo, H. Wu, L. Lin, Q. Liu, X. Han, Q. Xie, P. Liu, H. Zheng, L. Wang, X. Yu, D.-L. Peng, *Adv. Mater.* **2021**, *33*, 2005937.
[2] L. Wang, Z. Wu, J. Zou, P. Gao, X. Niu, H. Li, L. Chen, *Joule* **2019**, *3*, 2086.
[3] H.-H. Ryu, H. H. Sun, S.-T. Myung, C. S. Yoon, Y.-K. Sun, *Energy Environ. Sci.* **2021**, *14*, 844.
[4] J. Deng, C. Bae, A. Denlinger, T. Miller, *Joule* **2020**, *4*, 511.
[5] X. Zeng, M. Li, D. Abd El-Hady, W. Alshitari, A. S. Al-Bogami, J. Lu, K. Amine, *Adv. Energy Mater.* **2019**, *9*, 1900161.
[6] J. U. Choi, N. Voronina, Y.-K. Sun, S.-T. Myung, *Adv. Energy Mater.* **2020**, *10*, 2002027.
[7] W. Li, E. M. Erickson, A. Manthiram, *Nat. Energy* **2020**, *5*, 26.
[8] S. Zhao, K. Yan, J. Zhang, B. Sun, G. Wang, *Angew. Chem., Int. Ed.* **2021**, *60*, 2208.
[9] A. Manthiram, J. C. Knight, S.-T. Myung, S.-M. Oh, Y.-K. Sun, *Adv. Energy Mater.* **2016**, *6*, 1501010.
[10] Y. Zhang, Y. Katayama, R. Tatara, L. Giordano, Y. Yu, D. Fraggedakis, J. G. Sun, F. Maglia, R. Jung, M. Z. Bazant, Y. Shao-Horn, *Energy Environ. Sci.* **2020**, *13*, 183.
[11] L. Zou, W. Zhao, Z. Liu, H. Jia, J. Zheng, G. Wang, Y. Yang, J.-G. Zhang, C. Wang, *ACS Energy Lett.* **2018**, *3*, 2433.
[12] Y. S. Meng, G. Ceder, C. P. Grey, W. S. Yoon, M. Jiang, J. Bréger, Y. Shao-Horn, *Chem. Mater.* **2005**, *17*, 2386.
[13] W. Liu, P. Oh, X. Liu, M. J. Lee, W. Cho, S. Chae, Y. Kim, J. Cho, *Angew. Chem., Int. Ed.* **2015**, *54*, 4440.
[14] X. Liu, B. Zheng, J. Zhao, W. Zhao, Z. Liang, Y. Su, C. Xie, K. Zhou, Y. Xiang, J. Zhu, H. Wang, G. Zhong, Z. Gong, J. Huang, Y. Yang, *Adv. Energy Mater.* **2021**, *11*, 2003583.
[15] P. Yan, J. Zheng, M. Gu, J. Xiao, J.-G. Zhang, C.-M. Wang, *Nat. Commun.* **2017**, *8*, 14101.
[16] Y.-K. Sun, S.-T. Myung, B.-C. Park, J. Prakash, I. Belharouak, K. Amine, *Nat. Mater.* **2009**, *8*, 320.
[17] X. Xu, L. Xiang, L. Wang, J. Jian, C. Du, X. He, H. Huo, X. Cheng, G. Yin, *J. Mater. Chem. A* **2019**, *7*, 7728.
[18] H. Yang, H. H. Wu, M. Ge, L. Li, Y. Yuan, Q. Yao, J. Chen, L. Xia, J. Zheng, Z. Chen, J. Duan, K. Kisslinger, X. C. Zeng, W. K. Lee, Q. Zhang, J. Lu, *Adv. Funct. Mater.* **2019**, *29*, 1808825.
[19] W. Cho, Y. J. Lim, S.-M. Lee, J. H. Kim, J.-H. Song, J.-S. Yu, Y.-J. Kim, M.-S. Park, *ACS Appl. Mater. Interfaces* **2018**, *10*, 38915.
[20] F. Xin, H. Zhou, X. Chen, M. Zuba, N. Chernova, G. Zhou, M. S. Whittingham, *ACS Appl. Mater. Interfaces* **2019**, *11*, 34889.
[21] G. Hu, Y. Tao, Y. Lu, J. Fan, L. Li, J. Xia, Y. Huang, Z. Zhang, H. Su, Y. Cao, *ChemElectroChem* **2019**, *6*, 4773.
[22] B. Jin, Z. Cui, A. Manthiram, *Angew. Chem., Int. Ed.* **2023**, *62*, e202301241.
[23] N.-Y. Kim, J. Moon, M.-H. Ryou, S.-H. Kim, J.-H. Kim, J.-M. Kim, J. Bang, S.-Y. Lee, *Adv. Energy Mater.* **2021**, *12*, 2102109.
[24] H. Q. Pham, J. Lee, H. M. Jung, S.-W. Song, *Electrochim. Acta* **2019**, *317*, 711.
[25] B. Chang, J. Kim, Y. Cho, I. Hwang, M. S. Jung, K. Char, K. T. Lee, K. J. Kim, J. W. Choi, *Adv. Energy Mater.* **2020**, *10*, 2001069.
[26] Z. Xu, X. Guo, J. Wang, Y. Yuan, Q. Sun, R. Tian, H. Yang, J. Lu, *Adv. Energy Mater.* **2022**, *12*, 2201323.
[27] A. Banerjee, Y. Shilina, B. Ziv, J. M. Ziegelbauer, S. Luski, D. Aurbach, I. C. Halalay, *J. Electrochem. Soc.* **2017**, *164*, A6315.
[28] S.-J. Cho, K.-H. Choi, J.-T. Yoo, J.-H. Kim, Y.-H. Lee, S.-J. Chun, S.-B. Park, D.-H. Choi, Q. Wu, S.-Y. Lee, S.-Y. Lee, *Adv. Funct. Mater.* **2015**, *25*, 6029.
[29] Y. Tang, Y. Zhang, W. Li, B. Ma, X. Chen, *Chem. Soc. Rev.* **2015**, *44*, 5926.
[30] K. Lee, J. Lee, S. Choi, K. Char, J. W. Choi, *ACS Energy Lett.* **2018**, *4*, 94.
[31] Y. Wang, N. Dong, B. Liu, G. Tian, S. Qi, D. Wu, *Energy Stor. Mater.* **2023**, *56*, 621.
[32] R. Dominko, M. Gaberscek, J. Drofenik, M. Bele, S. Pejovnik, J. Jamnik, *J. Power Sources* **2003**, *119*, 770.
[33] S. Jaiser, M. Müller, M. Baunach, W. Bauer, P. Scharfer, W. Schabel, *J. Power Sources* **2016**, *318*, 210.
[34] L. Pfaffmann, S. Jaiser, M. Müller, P. Scharfer, W. Schabel, W. Bauer, F. Scheiba, H. Ehrenberg, *J. Power Sources* **2017**, *363*, 460.
[35] E. Zenkl, F. Stelzer, *J. Mol. Catal.* **1992**, *76*, 1.
[36] D. V. Mcgrath, R. H. Grubbs, J. W. Ziller, *J. Am. Chem. Soc.* **2002**, *113*, 3611.
[37] Y. Qiao, Y. Du, X. Zhang, Y. Li, *J. Appl. Polym. Sci.* **2017**, *134*, 45078.
[38] W. Haselrieder, B. Westphal, H. Bockholt, A. Diener, S. Höft, A. Kwade, *Int. J. Adhes. Adhes.* **2015**, *60*, 1.
[39] M. Fineman, S. D. Ross, *J. Polym. Sci.* **1950**, *5*, 259.
[40] S. C. Radzinski, J. C. Foster, R. C. Chapleski, D. Troya, J. B. Matson, *J. Am. Chem. Soc.* **2016**, *138*, 6998.
[41] C. W. Bielawski, D. Benitez, T. Morita, R. H. Grubbs, *Macromolecules* **2001**, *34*, 8610.
[42] J. J. Murphy, T. Kawasaki, M. Fujiki, K. Nomura, *Macromolecules* **2005**, *38*, 1075.
[43] Y. He, N. Liu, P. A. Kohl, *J. Electrochem. Soc.* **2020**, *167*, 067528.
[44] J. Lee, K. Lee, T. Lee, H. Kim, K. Kim, W. Cho, A. Coskun, K. Char, J. W. Choi, *Adv. Mater.* **2020**, *32*, 2001702.
[45] E. Barbu, R. A. Pullin, P. Graham, P. Eaton, R. J. Ewen, J. D. Smart, T. G. Nevell, J. Tsibouklis, *Polymer* **2002**, *43*, 1727.
[46] J. Tsibouklis, P. Graham, P. J. Eaton, J. R. Smith, T. G. Nevell, J. D. Smart, R. J. Ewen, *Macromolecules* **2000**, *33*, 8460.
[47] C. Toigo, M. Kracalik, E. Bradt, K. H. Pettinger, C. Arbizzani, *Polymers (Basel)* **2021**, *13*, 3582.
[48] L. Zhao, Y. Du, E. Zhao, C. Li, Z. Sun, Y. Li, H. Li, *Adv. Funct. Mater.* **2023**, 2214881.
[49] W. Xu, J. Long, J. Liu, H. Luo, H. Duan, Y. Zhang, J. Li, X. Qi, L. Chu, *Chem. Eng. J.* **2022**, *428*, 131203.
[50] Z. Lu, F. Sui, Y.-E. Miao, G. Liu, C. Li, W. Dong, J. Cui, T. Liu, J. Wu, C. Yang, *J. Energy Chem.* **2021**, *58*, 170.

[51] H. Yabu, M. Tanaka, K. Ijiro, M. Shimomura, *Langmuir* **2003**, *19*, 6297.
[52] K. Kim, S. Byun, I. Cho, M.-H. Ryou, Y. M. Lee, *ACS Appl. Mater. Interfaces* **2016**, *8*, 23688.
[53] B. Son, M.-H. Ryou, J. Choi, T. Lee, H. K. Yu, J. H. Kim, Y. M. Lee, *ACS Appl. Mater. Interfaces* **2014**, *6*, 526.
[54] D. Bouchard, W. Zhang, T. Powell, U.-S. Rattanaudompol, *Environ. Sci. Technol.* **2012**, *46*, 4458.
[55] J. H. Park, S. H. Sung, S. Kim, K. H. Ahn, *Ind. Eng. Chem. Res.* **2022**, *61*, 2100.
[56] X. Li, W. Peng, R. Tian, D. Song, Z. Wang, H. Zhang, L. Zhu, L. Zhang, *Electrochim. Acta* **2020**, *363*, 137185.
[57] B. Wang, J. Cui, Z. Li, H. Wang, D. Zhang, Q. Wang, H. Sun, Y. A. Wu, *Mater. Chem. Front.* **2023**, *7*, 2570.
[58] H. A. Kang, H. E. Bronstein, T. M. Swager, *Macromolecules* **2008**, *41*, 5540.
[59] X. Zhou, Z. Dai, S. Liu, J. Bao, Y.-G. Guo, *Adv. Mater.* **2014**, *26*, 3943.
[60] X. H. Rui, N. Ding, J. Liu, C. Li, C. H. Chen, *Electrochim. Acta* **2010**, *55*, 2384.
[61] N. Y. Hayley, H. Li, Y. S. Meng, S. Kumar, J. Breger, C. P. Grey, Y. Shao-Horn, *Chem. Mater.* **2007**, *19*, 2551.
[62] X. Wang, M. Zhang, J. Alvarado, S. Wang, M. Sina, B. Lu, J. Bouwer, W. Xu, J. Xiao, J.-G. Zhang, J. Liu, Y. S. Meng, *Nano Lett.* **2017**, *17*, 7606.
[63] S.-K. Jung, H. Gwon, J. Hong, K.-Y. Park, D.-H. Seo, H. Kim, J. Hyun, W. Yang, K. Kang, *Adv. Energy Mater.* **2014**, *4*, 1300787.
[64] A. E. Abdel-Ghany, A. M. Hashem, A. Mauger, C. M. Julien, *J. Solid State Electrochem.* **2020**, *24*, 3157.
[65] J. Wandt, C. Marino, H. A. Gasteiger, P. Jakes, R.-A. Eichel, J. Granwehr, *Energy Environ. Sci.* **2015**, *8*, 1358.
[66] D. Hu, Y. Su, L. Chen, N. Li, L. Bao, Y. Lu, Q. Zhang, J. Wang, S. Chen, F. Wu, *J. Energy Chem.* **2021**, *58*, 1.
[67] S. Kim, S. O. Park, M.-Y. Lee, J.-A. Lee, I. Kristanto, T. K. Lee, D. Hwang, J. Kim, T.-U. Wi, H.-W. Lee, S. K. Kwak, N.-S. Choi, *Energy Stor. Mater.* **2022**, *45*, 1.
[68] W. Zhao, J. Zheng, L. Zou, H. Jia, B. Liu, H. Wang, M. H. Engelhard, C. Wang, W. Xu, Y. Yang, J.-G. Zhang, *Adv. Energy Mater.* **2018**, *8*, 1800297.
[69] X. Xiong, D. Ding, Y. Bu, Z. Wang, B. Huang, H. Guo, X. Li, *J. Mater. Chem. A* **2014**, *2*, 11691.
[70] L. Xiao, X. Tang, Z. Ban, Z. Tang, H. Liu, C. Liu, Y. Lou, *Ionics* **2022**, *28*, 3101.
[71] W. Li, A. Dolocan, P. Oh, H. Celio, S. Park, J. Cho, A. Manthiram, *Nat. Commun.* **2017**, *8*, 14589.
[72] Z. Cui, Q. Xie, A. Manthiram, *Adv. Energy Mater.* **2021**, *11*, 2102421.
[73] S. Lee, W. Li, A. Dolocan, H. Celio, H. Park, J. H. Warner, A. Manthiram, *Adv. Energy Mater.* **2021**, *11*, 2100858.
[74] H. H. Sun, A. Dolocan, J. A. Weeks, A. Heller, C. B. Mullins, *ACS Nano* **2020**, *14*, 17142.
[75] H. Pei, Q. Yang, J. Yu, H. Song, S. Zhao, G. I. N. Waterhouse, J. Guo, S. Lu, *Small* **2022**, *18*, e2202037.
[76] N. Seehof, C. Mehler, S. Breunig, W. Risse, *J. Mol. Catal.* **1992**, *76*, 53.
[77] J. P. Cole, J. J. Lessard, C. K. Lyon, B. T. Tuten, E. B. Berda, *Polym. Chem.* **2015**, *6*, 5555.